



Contents lists available at ScienceDirect

## Combustion and Flame

journal homepage: [www.elsevier.com/locate/combustflame](http://www.elsevier.com/locate/combustflame)Kinetic modeling of total oxidation of propane over rhodium<sup>☆</sup>Ran Sui<sup>a,b,\*</sup>, John Mantzaras<sup>c</sup>, Zirui Liu<sup>b</sup>, Chung K. Law<sup>b</sup><sup>a</sup> Department of Mechanical and Aerospace Engineering, Missouri University of Science and Technology, Rolla, MO 65409, USA<sup>b</sup> Department of Mechanical and Aerospace Engineering, Princeton University, Princeton, NJ 08544, USA<sup>c</sup> Laboratory for Scientific Computing and Modeling, Paul Scherrer Institute, Villigen PSI, CH-5232, Switzerland

## ARTICLE INFO

## Article history:

Received 11 August 2021

Revised 23 October 2021

Accepted 24 October 2021

Available online xxx

## Keywords:

Catalytic combustion of propane

Rhodium catalyst

Surface kinetics

Pressure dependence of catalytic reactivity

VOC abatement

## ABSTRACT

The heat release rates of fuel-lean propane/air mixtures over a rhodium wire catalyst were measured with microcalorimetry experiments and simulated with a 2D reactive code. Based on these studies, global reaction parameters of the total oxidation of  $C_3H_8$  over Rh were extracted and a full catalytic reaction mechanism was developed. Wire microcalorimetry experiments were performed at atmospheric pressure and temperatures up to 900 K, while surface kinetic data was determined within the kinetic-controlled regime below 630 K. The dissociative adsorption of  $C_3H_8$  on Rh and its subsequent decomposition reaction were fitted based on the global reaction parameters, and a thermodynamically consistent reaction mechanism for the total oxidation of  $C_3H_8$  on Rh was constructed by incorporating these two fitted steps into a  $CH_4$ -Rh surface mechanism. The constructed catalytic reaction mechanism well reproduced the measured heat release rates in the wire microcalorimeter and was further validated against 2D Raman measurements of major gas-phase species concentrations in an Rh-coated planar channel. Moreover, when working in conjunction with a recently reported pressure dependence of catalytic reactivity and a detailed gas-phase chemistry, the developed catalytic reaction mechanism excellently captured the catalytic reactivity and the homogeneous ignition during hetero-/homogeneous combustion in the planar channel at pressures up to 6 bar. The hetero-/homogeneous coupling of the intermediate species (such as CO) appreciably affected the onset of homogeneous ignition, while the corresponding coupling via radical (O, H and OH) reactions was very weak. Finally, the key reactions controlling catalytic ignition and homogeneous ignition during hetero-/homogeneous combustion were identified.

© 2021 The Combustion Institute. Published by Elsevier Inc. All rights reserved.

## 1. Introduction

The catalytic total oxidation of propane ( $C_3H_8$ ) is of increasing importance in many industrial applications due to economic and environmental concerns. As a fuel, propane is the major component of liquefied petroleum gas (LPG, also known as “autogas”), which is readily accessible in compact containers for storage, transportation, and consumption, owing to its modest liquefaction temperatures and pressures. LPG-fueled vehicles have received extensive attention due to both low fuel costs and substantially reduced carbon and NOx emissions [1]; therein, unburnt propane in the exhaust is eliminated by catalytic converters [2]. Propane and LPG fuels are also attractive to micro- [3,4] and meso-scale [5,6] catalytic reactors for portable power generation. On the other hand, as a pollutant, propane is one of the most common and represen-

tative volatile organic compounds (VOC) [7,8]. Although propane itself is generally believed to be a green and nontoxic fuel, it reacts with hydroxyl radicals and produces tropospheric ozone, which is a toxic and strong greenhouse gas [9]. A rising trend in global atmospheric propane has been recently reported in the northern hemisphere, due to increased oil and natural gas production [10]. It is hence of importance to investigate the abatement of propane and other similar VOCs from industrial sources via catalytic combustion [11,12].

Among the commonly used noble metal catalysts, platinum has the highest reactivity toward the total oxidation of propane [13,14] and is also very resilient against sulfur poisoning. Nonetheless, rhodium has been widely used as a key promoter and additive in platinum- and palladium-based catalysts. For example, addition of Rh into Pt can promote the catalytic reactivity for the total oxidation of methane [15] and propane [16], while addition of Rh into Pd can improve the long term stability of the latter [17]. Furthermore, it has been recently reported that Rh also promotes propane oxidation over non-noble-metal catalysts [18].

Past studies of propane catalytic combustion over rhodium have primarily focused not on total but on partial oxidation, aiming at

<sup>☆</sup> Dedicated to Professor Katharina Kohse-Höinghaus on the occasion of her 70th birthday, in celebration of her distinguished contributions to combustion chemistry and diagnostics.

\* Corresponding author.

E-mail address: [rsui@mst.edu](mailto:rsui@mst.edu) (R. Sui).

hydrogen and syngas production. This is mainly due to rhodium's superior hydrogen and syngas selectivity during partial oxidation of hydrocarbons; the presence of hydrogen, in turn, facilitates the production of steam via homogeneous (gas-phase) reactions, which further accelerates the ensuing catalytic steam reforming [19]. In terms of kinetic studies, global reaction parameters over Rh/Al<sub>2</sub>O<sub>3</sub> catalysts [20] as well as detailed reaction mechanisms [21,22] have been developed for C<sub>3</sub>H<sub>8</sub> partial oxidation. For the total oxidation of C<sub>3</sub>H<sub>8</sub>, an effective activation energy of 74.7 kJ/mol was reported for Rh supported on YSZ (Yttria-Stabilized Zirconia) at atmospheric pressure [6]. In our recent study [23], a  $p^{0.14}$  pressure dependence of C<sub>3</sub>H<sub>8</sub> total oxidation on Rh was reported for the pressure range 1–6 bar and a global catalytic step with an effective activation energy of 78 kJ/mol was constructed. Moreover, when coupled to a homogeneous reaction mechanism, this global catalytic step captured the onset of gas-phase ignition in an Rh-coated channel [23]. Despite the above efforts, a detailed reaction mechanism for the total oxidation of C<sub>3</sub>H<sub>8</sub> over Rh is still missing, which hinders deeper understanding of the surface kinetics (e.g., knowledge of dominant surface coverage and of controlling reactions) and of the interactions between the catalytic and gaseous reaction pathways (e.g., coupling via adsorption/desorption reactions of radical and intermediate species). Consequently, the development and validation of such a surface mechanism constitutes the main objective of this work.

This paper is organized as follows. First, the adopted experimental and numerical microcalorimetry methodologies are introduced in Section 2. In Section 3 the global reaction parameters of C<sub>3</sub>H<sub>8</sub> total oxidation over Rh are reported, based on which two “lumped” steps are fitted and a detailed thermodynamically-consistent catalytic reaction mechanism is constructed. Subsequently, in Section 4 the developed reaction mechanism is validated against *in situ* Raman measurements of major gas-phase species concentrations and OH-PLIF measurements of homogeneous ignition in an Rh-coated rectangular channel. Finally, key reactions controlling catalytic ignition and homogeneous ignition during coupled hetero-/homogeneous combustion are identified in Section 5 and the main results are summarized in Section 6.

## 2. Experimental and numerical methodologies

Wire microcalorimetry experiments and CFD simulations were performed to assess the reaction parameters of C<sub>3</sub>H<sub>8</sub> total oxidation over Rh. The principle of wire microcalorimetry has been detailed elsewhere [24–26] and is hence only briefly described here. A polycrystalline Rh wire (purity 99.8%, supplied by Alfa Aesar, Thermo Fisher Scientific), 127  $\mu$ m in diameter and 100 mm in length, was positioned horizontally in the center of an enclosed rectangular chamber (Fig. 1), which had a horizontal cross-flow area of 200  $\times$  200 mm<sup>2</sup> and a height of 200 mm. The atmospheric-pressure gas environment was replenished with a creeping vertical gas flow at a constant speed of 15 mm/s. Such a low flow rate guaranteed catalytic heat release rates independent of the inlet gas velocity, as well as minimized flow separation, recirculation and upstream-to-downstream convective transport, when the wire temperature was maintained within a certain range. Consequently, the catalyst wire could be essentially considered as being immersed in a constant-concentration bath with uniform properties on the wire surface [24]. As shown in Fig. 2(a), the independence of heat release rate on inlet velocity held strictly at temperatures up to 630 K and inlet velocities of 10–25 mm/s.

The Rh wire was first heated in an air stream to a certain temperature  $T$ , by passing an electric current with power  $P_1(T)$ . The wire temperature, which was determined by a relation between its temperature and electric resistance [27], was real-time monitored and stable during data acquisition. Subsequently, a small amount of

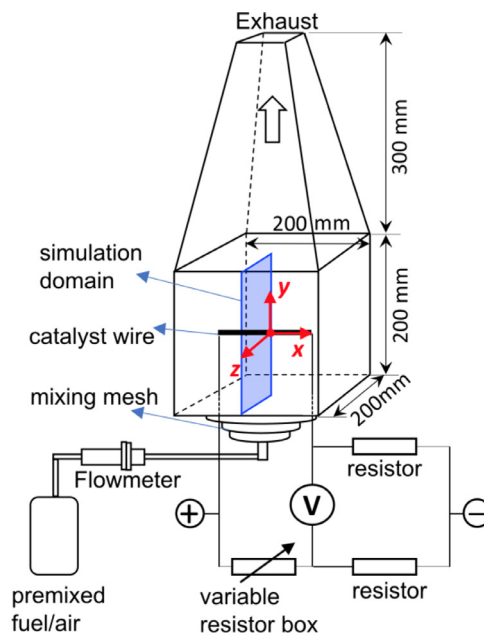
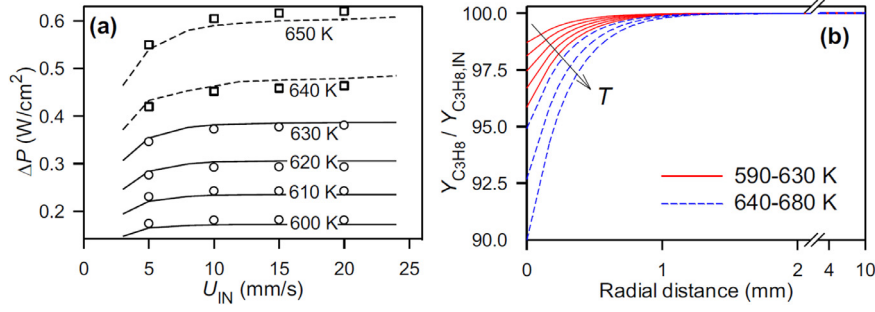


Fig. 1. Schematic of the wire microcalorimetry setup and the simulation domain.

fuel was introduced into the flow, thus creating a reactive mixture. Upon reaching a certain temperature, catalytic combustion was ignited and the surface heat release rate abruptly increased from zero. Accordingly, the electric heating power had to be adjusted to a lower value  $P_2(T)$  in order to maintain the same wire temperature  $T$ . Since the diffusive-convective heat loss from the wire to the gas environment was the same when the wire temperature was maintained at  $T$ , the difference in heating powers,  $\Delta P(T) = P_1 - P_2$ , yielded the catalytic heat release rate at this temperature. By varying  $T$ , a function  $\Delta P(T)$  was obtained, which subsequently provided the global reaction parameters. Experiments were performed at wire temperatures below 900 K. Such moderate catalyst temperatures, together with the minute surface-to-volume ratio of the reactor in Fig. 1, negated falsification of the extracted surface kinetic data from potential gaseous reactions –whose minimal impact was further confirmed by the simulations. Same as previous studies under similar operating conditions [6,23], partial oxidation products (H<sub>2</sub>, CO, CH<sub>4</sub> and C<sub>2</sub> species) were absent for the investigated ultra-lean stoichiometries at all investigated temperatures, as confirmed by gas chromatography measurements (Inficon 3000 micro-GC, sampled from exhaust gasses of the wire microcalorimeter).

In the numerical part, a 2D code (ANSYS Fluent 2021 R1) was employed in conjunction with detailed catalytic and gas-phase reaction mechanisms; the code has been validated against past wire microcalorimetry experiments [24,26,28,29]. The simulation domain comprised a rectangle of 200 mm  $\times$  100 mm (in  $-y$  and  $-z$ , respectively), normal to the wire (see Fig. 1). Symmetry boundary conditions were used at the domain's right side ( $z = 0$ ), prescribed values of all thermoscalars at the lower side ( $y = -100$  mm), zero-Neumann conditions at the top side ( $y = 100$  mm), while at the solid wall side ( $z = 100$  mm) no slip conditions and non-reactive walls at room temperature were considered. 164,224 body-fitted curvilinear cells, which were refined at near-wire regions with 80 grids over the modeled half wire periphery, yielded grid-independent solutions. Gravity in the  $y$ -direction was included in the simulations. In the present study, a detailed catalytic reaction mechanism for fuel-lean C<sub>3</sub>H<sub>8</sub> oxidation over Rh (Table 1, 14 surface species and 48 reactions) was developed based on the present wire microcalorimetry experiments and the CH<sub>4</sub>-Rh mechanism by



**Fig. 2.** (a) Measured (symbols) and computed (lines, using the reaction mechanism of Table 1) heat release rates of 1% vol.  $C_3H_8$  in air at 600–650 K and 3–24 mm/s inlet velocities. (b) Computed normalized radial profiles of  $C_3H_8$  mass fraction  $Y_{C_3H_8}/Y_{C_3H_8,IN}$  at temperatures 590–630 K (solid lines) and 640–680 K (dashed lines), inlet velocity 15 mm/s.

**Table 1**

Surface reaction mechanism of the total oxidation of  $C_3H_8$  over Rh\*.

No.	Reaction	A	b	$E_a$
1	$C_3H_8 + Rh(s) + O(s) \rightarrow C_3H_7(s) + OH(s)$	$1.3 \times 10^{22}$	0	45.9
2	$C_3H_7(s) + 2Rh(s) \rightarrow CH_3(s) + 2CH_2(s)$	$2.9 \times 10^{30}$	0	82
3	$O_2 + 2Rh(s) \rightarrow 2O(s)$	$1.0 \times 10^{-2} (\gamma)$	0	0
4	$2O(s) \rightarrow 2Rh(s) + O_2$	$5.33 \times 10^{22}$	-0.137	387
5	$H_2 + 2Rh(s) \rightarrow 2H(s)$	$3.0 \times 10^{-2} (\gamma)$	0	0
6	$2H(s) \rightarrow 2Rh(s) + H_2$	$5.57 \times 10^{19}$	0.239	59.69
7	$CO + Rh(s) \rightarrow CO(s)$	$4.97 \times 10^{-1} (\gamma)$	0	0
8	$CO(s) \rightarrow Rh(s) + CO$	$1.3 \times 10^{13}$	0.295	$134.07-47\theta_{CO(s)}$
9	$H_2O + Rh(s) \rightarrow H_2O(s)$	$1.0 \times 10^{-1} (\gamma)$	0	0
10	$H_2O(s) \rightarrow Rh(s) + H_2O$	$6.86 \times 10^{14}$	-0.280	44.99
11	$CO_2 + Rh(s) \rightarrow CO_2(s)$	$4.8 \times 10^{-2} (\gamma)$	0	0
12	$CO_2(s) \rightarrow Rh(s) + CO_2$	$3.92 \times 10^{11}$	0.315	20.51
13	$O(s) + H(s) \rightarrow OH(s) + Rh(s)$	$8.83 \times 10^{21}$	-0.048	73.365
14	$OH(s) + Rh(s) \rightarrow O(s) + H(s)$	$1.0 \times 10^{21}$	0.045	48.04
15	$OH(s) + H(s) \rightarrow H_2O(s) + Rh(s)$	$1.74 \times 10^{22}$	-0.127	41.73
16	$H_2O(s) + Rh(s) \rightarrow OH(s) + H(s)$	$5.41 \times 10^{21}$	0.129	98.22
17	$OH(s) + OH(s) \rightarrow O(s) + H_2O(s)$	$5.74 \times 10^{20}$	-0.081	121.59
18	$O(s) + H_2O(s) \rightarrow OH(s) + OH(s)$	$1.57 \times 10^{22}$	0.081	203.41
19	$O(s) + C(s) \rightarrow CO(s) + Rh(s)$	$1.17 \times 10^{22}$	0	$92.14-120\theta_{C(s)}$
20	$CO(s) + Rh(s) \rightarrow O(s) + C(s)$	$6.39 \times 10^{21}$	0	$174.76-47\theta_{CO(s)}$
21	$O(s) + CO(s) \rightarrow CO_2(s) + Rh(s)$	$6.18 \times 10^{21}$	0.034	$129.98-47\theta_{CO(s)}$
22	$CO_2(s) + Rh(s) \rightarrow O(s) + CO(s)$	$5.75 \times 10^{21}$	-0.175	106.49
23	$CO(s) + OH(s) \rightarrow COOH(s) + Rh(s)$	$2.92 \times 10^{20}$	0	$55.33-47\theta_{CO(s)}$
24	$COOH(s) + Rh(s) \rightarrow CO(s) + OH(s)$	$2.74 \times 10^{21}$	0	48.38
25	$COOH(s) + Rh(s) \rightarrow CO_2(s) + H(s)$	$1.17 \times 10^{19}$	0.160	5.61
26	$CO_2(s) + H(s) \rightarrow COOH(s) + Rh(s)$	$1.16 \times 10^{20}$	-0.160	14.48
27	$COOH(s) + H(s) \rightarrow CO(s) + H_2O(s)$	$6.00 \times 10^{19}$	-0.188	33.55
28	$CO(s) + H_2O(s) \rightarrow COOH(s) + H(s)$	$2.26 \times 10^{19}$	0.051	$97.08-47\theta_{CO(s)}$
29	$CO(s) + OH(s) \rightarrow CO_2(s) + H(s)$	$3.07 \times 10^{19}$	0	$82.94-47\theta_{CO(s)}$
30	$CO_2(s) + H(s) \rightarrow CO(s) + OH(s)$	$2.50 \times 10^{21}$	-0.301	84.77
31	$C(s) + OH(s) \rightarrow CO(s) + H(s)$	$4.22 \times 10^{21}$	0.078	$30.04-120\theta_{C(s)}$
32	$CO(s) + H(s) \rightarrow C(s) + OH(s)$	$3.24 \times 10^{21}$	-0.078	$138.26-47\theta_{CO(s)}$
33	$CH_4(s) + Rh(s) \rightarrow CH_3(s) + H(s)$	$4.62 \times 10^{21}$	0.136	72.26
34	$CH_3(s) + H(s) \rightarrow CH_4(s) + Rh(s)$	$2.14 \times 10^{21}$	-0.058	46.77
35	$CH_3(s) + Rh(s) \rightarrow CH_2(s) + H(s)$	$1.28 \times 10^{24}$	0.078	107.56
36	$CH_2(s) + H(s) \rightarrow CH_3(s) + Rh(s)$	$1.07 \times 10^{22}$	-0.078	39.54
37	$CH_2(s) + Rh(s) \rightarrow CH(s) + H(s)$	$1.28 \times 10^{24}$	0.078	115.39
38	$CH(s) + H(s) \rightarrow CH_2(s) + Rh(s)$	$1.07 \times 10^{22}$	-0.078	52.61
39	$CH(s) + Rh(s) \rightarrow C(s) + H(s)$	$1.46 \times 10^{20}$	0.078	23.09
40	$C(s) + H(s) \rightarrow CH(s) + Rh(s)$	$1.12 \times 10^{23}$	-0.078	$170.71-120\theta_{C(s)}$
41	$CH_4(s) + O(s) \rightarrow CH_3(s) + OH(s)$	$3.47 \times 10^{23}$	0.051	77.71
42	$CH_3(s) + OH(s) \rightarrow CH_4(s) + O(s)$	$1.82 \times 10^{22}$	-0.051	26.89
43	$CH_3(s) + O(s) \rightarrow CH_2(s) + OH(s)$	$4.79 \times 10^{24}$	0	114.52
44	$CH_2(s) + OH(s) \rightarrow CH_3(s) + O(s)$	$2.86 \times 10^{21}$	0	20.88
45	$CH_2(s) + O(s) \rightarrow CH(s) + OH(s)$	$4.79 \times 10^{24}$	0	141.79
46	$CH(s) + OH(s) \rightarrow CH_2(s) + O(s)$	$2.86 \times 10^{21}$	0	53.41
47	$CH(s) + O(s) \rightarrow C(s) + OH(s)$	$5.01 \times 10^{20}$	0	26.79
48	$C(s) + OH(s) \rightarrow CH(s) + O(s)$	$2.73 \times 10^{22}$	0	$148.81-120\theta_{C(s)}$

\* Reaction rates are  $k = A^b \exp(E_a/RT)$  with activation energy  $E_a$  (kJ/mol).  $\gamma$  denotes sticking coefficients. The surface site density is  $\Gamma = 2.72 \times 10^{-9}$  mol/cm<sup>2</sup>. For reactions among surface species, the units of pre-exponential factors A are mol<sup>(1-m)</sup>cm<sup>2(m-1)</sup>s<sup>-1</sup>K<sup>-b</sup>, with m denoting the reaction order based on all surface reactants. For adsorption reactions which are not expressed in terms of a sticking coefficient, the units of A are mol<sup>(1-m-n)</sup>cm<sup>2(m-1)+3n</sup>s<sup>-1</sup>K<sup>-b</sup>, with n denoting the reaction order based on all gaseous reactants. Reactions 1 and 2 were developed in this work. All the other reactions were taken from [30] without change.

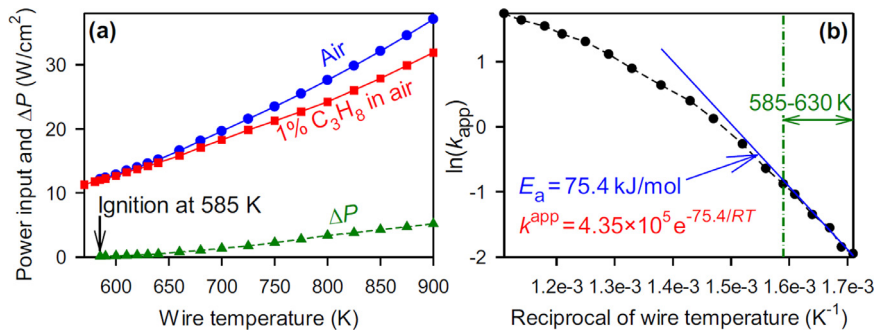


**Fig. 3.** (a) Electrical power inputs needed to maintain Rh wire in air (circles) and reactive mixture (1% vol. C<sub>3</sub>H<sub>8</sub> in air, squares) flows. The differences yield the catalytic heat release rates  $\Delta P$  (triangles). (b) Arrhenius plot of (a): experimental data (symbols and dashed line) and linear fit (solid line).

Karakaya et al. [30]. For C<sub>3</sub>H<sub>8</sub> gas-phase chemistry, the latest San Diego mechanism [31] (58 species and 268 reactions) was adopted, along with its thermodynamic and transport databases. Mixture-averaged species transport model was used by Fluent. As mentioned before, the gas-phase chemistry in the simulations ensured the absence of gas-phase ignition, which would otherwise falsify the extraction of surface kinetics.

### 3. Development of surface kinetic model

#### 3.1. Extraction of global reaction parameters

Global reaction parameters of C<sub>3</sub>H<sub>8</sub> total oxidation over Rh were first obtained from the heat release measurements. To ensure negligible changes in the heat transfer properties of the reactive mixtures and air [25], only 0.5–1.0% vol. C<sub>3</sub>H<sub>8</sub> was doped into air (300 K), resulting in fuel-to-air equivalence ratios  $\varphi = 0.12$ –0.24. As shown in Fig. 3(a), the observed catalytic ignition temperature of C<sub>3</sub>H<sub>8</sub> on Rh was around 585 K, close to the past measurement of 573 K in an annular microreactor [22] (this comparison is meaningful even though [22] referred to partial oxidation, since total oxidation is first triggered, followed by partial oxidation). Data was extracted within the kinetic-controlled regime at temperatures up to 630 K, above which reactions became fast and fell into the mixed kinetic/transport-controlled regime. As shown in Fig. 2(a), below 630 K (circles and solid lines, kinetic-controlled regime) both measured and predicted heat release rates were independent of the inlet velocity. In contrast, a trend of increasing heat release rate with increasing inlet velocity was observed at temperatures above 640 K (squares and dashed lines), which was progressively aggravated at higher temperatures. This behavior was further confirmed by the computed radial profiles of the C<sub>3</sub>H<sub>8</sub> mass fraction  $Y_{C_3H_8}$  near the Rh wire in Fig. 2(b), normalized by the inlet C<sub>3</sub>H<sub>8</sub> mass fraction  $Y_{C_3H_8,IN}$ . It is seen that below 630 K the near-wall ratios in Fig. 2(b) were well-above 95%, thus manifesting a strong kinetic-controlled regime with negligible external diffusion limitations within the low-temperature range where the surface kinetics was evaluated. The profiles in Fig. 2(b) were largely similar for all azimuthal positions around the wire, since gravity did not significantly affect them.

The measured heat release rates for the case with 1% vol. C<sub>3</sub>H<sub>8</sub> in air and the corresponding Arrhenius plot are shown in Fig. 3. Considering that O<sub>2</sub> is in large excess, the apparent reaction rate of C<sub>3</sub>H<sub>8</sub> total oxidation can be expressed as:

$$\dot{s}_{C_3H_8} = \Delta P / \Delta H_r = k^{app} [C_3H_8]_w, \quad (\text{mol/cm}^2/\text{s}) \quad (1)$$

where  $\Delta H_r$  denotes the enthalpy of combustion of C<sub>3</sub>H<sub>8</sub> (lower heating value) and the subscript w the gas/solid interface. Such a global step, first-order with respect to C<sub>3</sub>H<sub>8</sub> and zeroth-order with

respect to O<sub>2</sub>, was shown valid under similar conditions of C<sub>3</sub>H<sub>8</sub> total oxidation in our recent study [23].

The global rate of C<sub>3</sub>H<sub>8</sub>/air total oxidation over Rh was deduced from Arrhenius plots and averaged from the 0.5–1.0% vol. C<sub>3</sub>H<sub>8</sub> cases (for brevity, the 0.5% vol. results are not included in Fig. 3). The apparent activation energy  $E_a$  and the pre-exponential factor  $A$  were deduced from the negative slope and extrapolation of the y-intercept of the  $\ln(k^{app})$  versus  $1/T$  plot over the kinetic-controlled regime, respectively. Consequently, the obtained global step has the following reaction coefficients:

$$k^{app} = (4.35 \pm 0.45) \times 10^5 e^{-(75.4 \pm 1.1) (\text{kJ/mol})/RT} (\text{cm/s}) \quad (2)$$

The derived global activation energy, 75.4 kJ/mol, was in good agreement with past studies: for total oxidation, 74.7 kJ/mol was obtained in a heat recirculating meso-scale combustor [6] and 78 kJ/mol in a planar flow reactor [23], while for partial oxidation 80 kJ/mol was reported in a honeycomb reactor [20].

Surface characterization of the Rh catalyst was accomplished via X-ray Photoelectron Spectroscopy (XPS) and Energy-dispersive X-ray spectroscopy (EDX). XPS measurements involved a VG Scientific ESCALAB 220iXL spectrometer (Thermo Fisher Scientific) using focused monochromatized Al K $\alpha$  radiation (1486.6 eV) and were performed ex situ on 10 × 10 mm<sup>2</sup> samples (2.2- $\mu$ m-thick Rh layer coated on non-porous Al<sub>2</sub>O<sub>3</sub> via plasma vapor deposition), which were heated in air in an atmospheric-pressure oven for 1 hr. The considerably thick noble metal coating closely resembled a polycrystalline surface and excluded support effects [32]. The Rh 3d regions of samples heated at various temperatures are illustrated in Fig. 4(a). The 3d<sub>5/2</sub> peaks are at 307.2 and 308.3 eV for Rh<sup>0</sup> (metallic) and Rh<sup>3+</sup> (Rh<sub>2</sub>O<sub>3</sub>), respectively. Similarly, the 3d<sub>3/2</sub> peaks are at 311.8 and 313.1 eV for Rh<sup>0</sup> and Rh<sup>3+</sup>, respectively [33]. The spectra indicated that both metallic and oxidized rhodium phases existed below and above the ignition temperature of C<sub>3</sub>H<sub>8</sub> on the catalyst surface (see the curves of 573 K and 623 K), and the oxidized phase became dominant when the samples were heated above 750 K. Such a phase change was also reflected by the O 1s spectra (peak at 529.9 eV) in Fig. 4(b). It is worth mentioning that the transition from mixed metallic/oxidized to fully oxidized phase does not necessitate a more complex reaction mechanism with more than one active rhodium sites, probably due to the fast replenishment of oxygen vacancy by the excess gas-phase oxygen under the present fuel-lean environment [34]. Such a single type of active site Rh(s) was also attested by the Deutschmann group in their kinetic modeling of CH<sub>4</sub> oxidation on Rh, which was validated against tests in an annular flow reactor over the wider temperature range 573–1123 K [30]. The dominance of oxidized phase was accentuated at even higher temperatures, as illustrated with the EDX measurements in Figs. 4(c) and 4(d), where the oxygen concentration increased from 2.0% at 750 K to 7.7% at 1000 K.



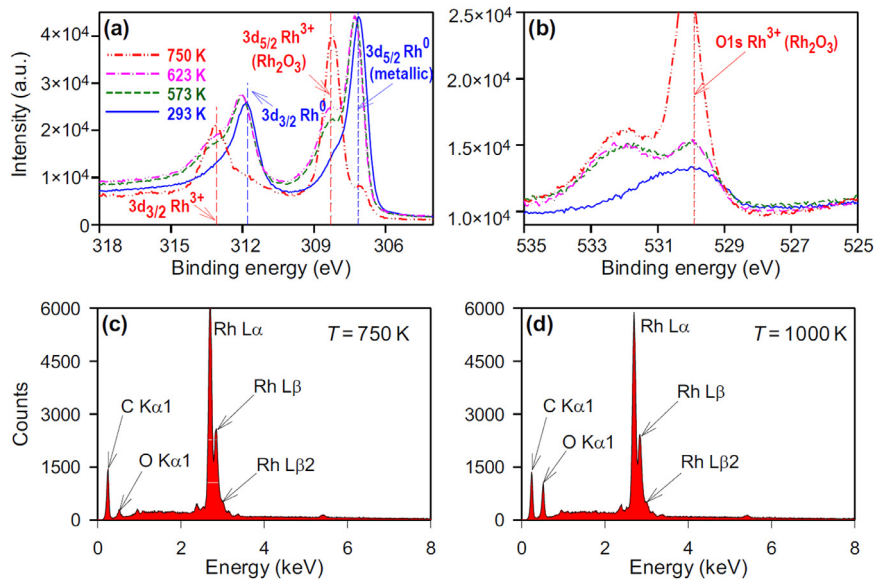


**Fig. 4.** XPS spectra ((a) Rh 3d and (b) O 1s regions) of samples heated to 293, 573, 623 and 750 K, and EDX spectra of samples heated to 750 K (c) and 1000 K (d).

### 3.2. Construction of a detailed catalytic reaction mechanism

The adsorption of  $C_3H_8$  and its subsequent surface decomposition step were fitted as two “lumped” reactions, based on the global step of  $C_3H_8$  total oxidation derived in Section 3.1. A detailed reaction mechanism for the total oxidation of  $C_3H_8$  on Rh (Table 1) was subsequently constructed by incorporating these two steps with a literature  $CH_4$ -Rh reaction mechanism [30], which had been validated for both total and partial oxidation. The  $CH_4$  adsorption/desorption steps of [30] were not included in the constructed reaction mechanism, as they would otherwise generate unrealistic amounts of  $CH_4$  in the products due to the considerably lower desorption activation energy of  $CH_4$  compared to  $H_2O$ . The same issue also appeared in [23] when attempting to use the CPO-tuned detailed surface mechanism of  $C_3H_8$  on Rh [21] for the simulation of  $C_3H_8$  total oxidation; it was reported [23] that this mechanism resulted in the formation of large amounts of  $CH_4$  (and also of  $H_2$  and  $CO$ ), which were however absent in the total oxidation experiments.

The use of main reactions from the  $CH_4$  mechanism [30] was greatly facilitated by the fact that after the dissociative  $C_3H_8$  adsorption and subsequent decomposition, only  $C_1$  surface species ( $CH_3(s)$  and  $CH_2(s)$ ) were present. This approach of adding “lumped” steps for the surface adsorption and decomposition of  $C_{2+}$  species has been successfully adopted by various groups for the partial oxidation of  $C_3H_8$  [22] and  $isoC_8H_{18}$  [35] on Rh, and the total oxidation of  $C_3H_8$ ,  $C_2H_6$  and  $C_2H_4$  on Pd [28,36].

Same as the past study of the total oxidation of  $C_3H_8$  on Pd [28], in the present work the dissociative adsorption of  $C_3H_8$  on Rh and its subsequent decomposition step (reactions R1 and R2 of Table 1) were modeled as  $C_3H_8 + Rh(s) + O(s) \rightarrow C_3H_7(s) + OH(s)$  and  $C_3H_7(s) + 2Rh(s) \rightarrow CH_3(s) + 2CH_2(s)$ , respectively. With R1 being the only “elementary” step involving  $C_3H_8$ , the overall conversion rate of  $C_3H_8$  can be expressed as

$$\dot{C}_{C_3H_8} = k^{app}[C_3H_8]_w = k_1[C_3H_8]_w(\Gamma\theta_{Rh(s)})(\Gamma\theta_{O(s)}) \quad (3)$$

where  $\Gamma$  denotes the surface site density of the catalyst, while  $\theta_{Rh(s)}$  and  $\theta_{O(s)}$  are the free surface site and O-occupied site fractions, respectively.

Since R1 and R2 are the only reactions producing/consuming  $C_3H_7(s)$ , whose net catalytic molar production rate ought to be

zero at steady state [37], recognizing that all present experiments are steady state, these two reactions could be linked via

$$\dot{C}_{C_3H_7(s)} = k_1[C_3H_8]_w(\Gamma\theta_{Rh(s)})(\Gamma\theta_{O(s)}) - k_2(\Gamma\theta_{Rh(s)})^2(\Gamma\theta_{C_3H_7(s)}) = 0 \quad (4)$$

Eqs. (3) and (4) further yielded the reaction rates of R1 and R2 as

$$k_1 = \frac{k^{app}}{\Gamma^2\theta_{Rh(s)}\theta_{O(s)}} \quad (5)$$

$$k_2 = \frac{k_1[C_3H_8]_w\theta_{O(s)}}{\Gamma\theta_{Rh(s)}\theta_{C_3H_7(s)}} \quad (6)$$

The derived rate expressions in Eqs. (5) and (6) were implicitly coupled with the unknown surface fractions of  $Rh(s)$ ,  $O(s)$  and  $C_3H_7(s)$ . Hence,  $k_1$  and  $k_2$  were determined iteratively using Fluent simulations. The iterative procedure is as follows: an initial guess of  $k_1$  and  $k_2$  (based on the same reactions on Pd from [28] and tuned to match the heat release measurements) was used in the first iteration, from which the surface fractions of  $Rh(s)$ ,  $O(s)$  and  $C_3H_7(s)$  were obtained.  $k_1$  and  $k_2$  were subsequently updated using Eqs. (5) and (6), where  $k^{app}$  was determined as in Eq. (2). The pre-exponential factors and activation energies of R1 and R2 were obtained from the Arrhenius plots of  $k_1$  and  $k_2$ , and then used in the next iteration. The iterative procedure was repeated until the values of  $k_1$  and  $k_2$  converged. Thermodynamic consistency of the developed reaction mechanism in Table 1 was satisfied with an overall energy balance (from gaseous  $C_3H_8$  and  $O_2$  to  $H_2O$  and  $CO_2$ ) error less than 1.7%. The small error in thermodynamic consistency could be completely eliminated by increasing the activation energies of R1 and R2, which could however lead to inaccurate predictions of the heat release rates, especially at low temperature ranges. It is noted that the aforementioned small error in the thermodynamic consistency had no effect on the simulations of the present steady experiments. In steady simulations, the heat release rate is solely determined by the energetics of the adsorbing/desorbing gaseous species and not by the energetics of the surface species, whose reaction rates are identically zero (see e.g. Eq. (4)) [38]. The aforementioned 1.7% error, however, could have a small impact in simulations of transient experiments. It is finally worth mentioning that, even though backward reactions are

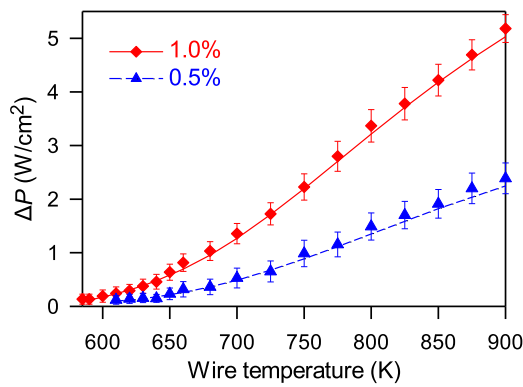


**Fig. 5.** Measured (symbols) and predicted (lines, using the reaction mechanism of Table 1) heat release rates of 1.0% (diamonds, solid line) and 0.5% (triangles, dashed lines) vol.  $C_3H_8$  in air over the Rh wire.

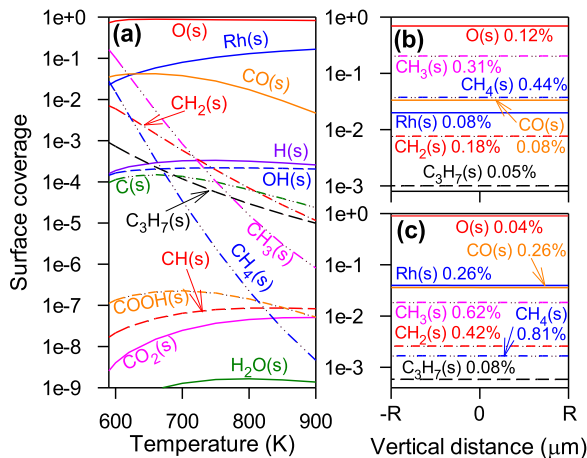


**Fig. 6.** (a) Computed surface species coverage (averaged over the Rh wire surface) for 1.0%  $C_3H_8$  in air at 585–900 K. (b-c) Surface coverage of major species and the peak azimuthal deviations over the modeled half cross-sectional wire perimeter (from  $-R$  to  $R$ , where  $R$  is the wire cross sectional diameter and 0 the vertical position of the circle center) at 585 K (b) and 630 K (c).

not included in the “lumped” reactions and the constructed mechanism, fuel desorption steps are typically negligible compared to adsorption after ignition under steady-state and fuel-lean conditions [39,40].

Predictions with the constructed reaction mechanism reproduced excellently the measured heat release rates of 0.5 and 1.0% vol.  $C_3H_8$  doped in air over the Rh wire at all investigated temperatures, as shown in Fig. 5. Computed surface coverage (azimuthally averaged over the catalyst wire surface) for the 1.0% case is provided in Fig. 6(a). Surface oxygen is dominant over the entire temperature range, while  $CH_3(s)$ ,  $CH_4(s)$  and  $CO(s)$  are also abundant within the kinetic-controlled regime up to  $\sim 630$  K, above which free site  $Rh(s)$  overtakes them.  $C_3H_7(s)$ ,  $CH_2(s)$ ,  $CH_3(s)$  and  $CH_4(s)$  decrease drastically with rising temperatures and are all surpassed by  $H(s)$  and  $OH(s)$  below  $\sim 740$  K. Figs. 6(b) and 6(c) provide computed coverage of major surface species along the perimeter of the simulated half-wire circle (i.e., wire cross section, see Fig. 1) at two temperatures 585 and 630 K, both within the kinetic-controlled regime. It is clear that at both temperatures all the surface species are uniformly distributed over the wire surface (with deviations 0.04–0.81%), thus re-confirming the assumption that within the kinetic-controlled regime uniform properties are guaranteed on the wire surface with the adopted low flow rates. At all temperatures,  $O(s)$  and  $Rh(s)$  were main surface species, with the latter increasing with rising temperature.

#### 4. Validation of the developed catalytic model with planar flow reactor tests

The developed catalytic reaction mechanism in Table 1 was further validated against our recently reported laser-based measurements of steady  $C_3H_8$  total oxidation in an Rh-coated channel-flow reactor [23]. The test-rig and measuring techniques have been detailed in past studies [40,41] and are only briefly described here. The rectangular channel reactor comprised two 9-mm-thick horizontal Si[SiC] ceramic plates having a streamwise ( $-x$ ) length of 300 mm, a lateral ( $-z$ ) width of 104 mm, and two 3-mm-thick vertical quartz windows that maintained a vertical ( $-y$ ) separation of 7 mm between the two plates. The inner  $300 \times 104$  mm<sup>2</sup> ceramic plate surfaces were coated with a 2.2- $\mu$ m-thick polycrystalline Rh layer using plasma vapor deposition, while the plate temperatures were controlled by a combined heating/cooling arrangement comprising two adjustable-power resistive coils in the rear plate sections and two cooling air jets in the front plate sections. The catalyst temperatures were measured along the  $x$ - $y$  symmetry plane of the channel by 12 S-type thermocouples for each plate, which were positioned 0.9 mm beneath the catalytically coated surfaces. 1D Raman measurements of major gaseous species concentrations over the 7 mm channel height accessed the catalytic processes at five selected axial positions  $x = 8, 36, 66, 96$  and 126 mm, while planar laser induced fluorescence (PLIF) of the OH radical along the  $x$ - $y$  symmetry plane monitored gas-phase ignition.

As listed in Table 2, selected cases from [23] were simulated using the reaction mechanism of Table 1. Raman measurements were performed in Cases 1–3, in which homogeneous combustion was negligible. The catalyst temperatures over the range of Raman measurements in Cases 1–3 were modestly higher than the wire microcalorimetry experiments (by  $\sim 100$  K), while the inlet equivalence ratio was close to the upper limit value of the wire microcalorimetry experiments ( $\phi = 0.24$  when 1.0%  $C_3H_8$  was doped in air). In Cases 4–6 homogeneous combustion was ignited and monitored by OH-PLIF; homogeneous combustion was achieved as a result of the increased wall temperatures, increased residence times (reduced inlet velocities) and increased inlet equivalence ratios. Experiments were performed at pressures of 1–6 bar [23] and a global pressure dependence of catalytic reactivity  $p^{0.14}$  was reported for the total oxidation of  $C_3H_8$  on Rh based on the following one-step reaction:

$$\dot{s}_{C_3H_8} = A \left( \frac{p}{p_0} \right)^{-n} \exp \left( \frac{-E_a}{RT_w} \right) [C_3H_8]_w \quad (7)$$

where  $p_0 = 1$  bar is the reference pressure and  $n = 0.86$  the pressure exponent that restrained the increase of the catalytic reaction rate with rising pressure. The overall pressure dependence of the catalytic reactivity  $\dot{s}_{C_3H_8}$  in Eq. (7) is  $\sim p^{1-n}$  since the interfacial gas/wall  $C_3H_8$  concentration  $[C_3H_8]_w \sim p$ . Although the catalytic reaction mechanism of Table 1 was developed under atmospheric pressure (in both wire microcalorimetry experiments and the original  $CH_4$  mechanism [30]), it excellently reproduced the measured catalytic reactivity and homogeneous ignition when all surface reactions were uniformly scaled with the  $(p/p_0)^{-0.86}$  factor in the simulations. This implied multiplication of all pre-exponentials  $A$  in Table 1 by  $(p/p_0)^{-0.86}$ .

Our proprietary 2D steady Navier-Stokes reactive code [32] was used to simulate the channel flow experiments in Table 2. A staggered grid with  $480 \times 68$  points (in  $x$  and  $y$  directions, respectively) for the  $300 \times 7$  mm<sup>2</sup> domain was sufficient to produce grid-independent solutions. Uniform inlet velocities, gas species concentrations and temperature were applied at the channel entry, while the upper ( $y = 7$  mm) and lower ( $y = 0$  mm) wall temperatures were prescribed (by fitting axial temperature profiles through the 12 thermocouple measurements on each Si[SiC] plate). The

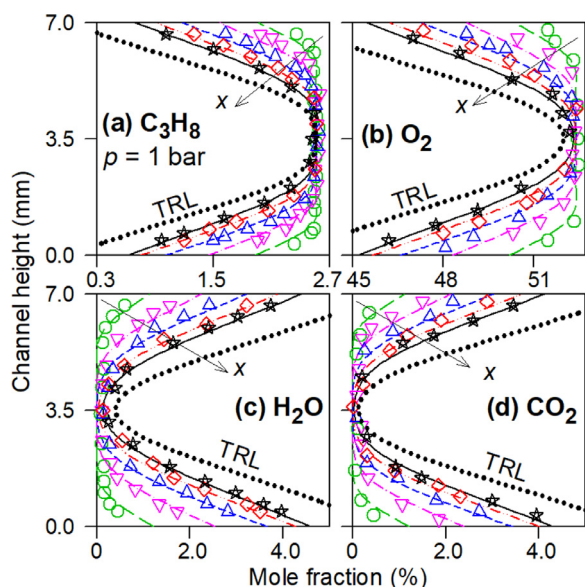


**Fig. 7.** Raman measured (symbols) and simulated (lines, using the reaction mechanism of Table 1) transverse profiles of  $C_3H_8$ ,  $O_2$ ,  $H_2O$  and  $CO_2$  for Case 1 at 1 bar;  $x = 8$  mm (circles, long dashed lines), 36 mm (lower triangles, dashed dotted lines), 66 mm (upper triangles, short dashed lines), 96 mm (diamonds, dashed double-dotted lines), and 126 mm (stars, solid lines). Thick dotted lines marked TRL denote the predicted transport-limited solutions at  $x = 126$  mm.

catalytic reaction mechanism of Table 1 was applied together with the San Diego gas-phase mechanism [31], although gas-phase combustion was not ignited in Cases 1–3. Surface and gas-phase reaction rates were evaluated with Chemkin [42,43], while a mixture-averaged species transport model [44] was used.

The catalytic reaction mechanism of Table 1 reproduced well all the Raman-measured major reactive gaseous species concentrations in Cases 1–3. Gas-phase combustion was not initiated in these cases as confirmed by both the simulations in this work and the OH-PLIF measurements in [23], thus excluding potential falsification of the surface kinetics by gas-phase chemistry. Measured and predicted transverse profiles of  $C_3H_8$ ,  $O_2$ ,  $H_2O$  and  $CO_2$  for Case 1 at the five selected axial locations are presented in Fig. 7. The thick dotted lines marked TRL denote transport-limited (i.e., infinitely fast chemistry) simulations for the last axial location at  $x = 126$  mm, demarcating the lower/upper physical limits of the reactants/products. In [23]  $C_3H_8$  and  $H_2O$  profiles were also well predicted for pressures below 2 bar by a detailed reaction mechanism for  $C_3H_8$  partial oxidation developed in [21]. However, this mechanism failed to predict  $O_2$  and  $CO_2$  and resulted in unrealistic amounts of partial oxidation products ( $CO$ ,  $H_2$  and  $CH_4$ ).

Although the present catalytic reaction mechanism was developed for atmospheric pressure, when scaled with the  $p^{-0.86}$  pressure dependence in the simulations, it captured closely the measured catalytic reactivity in Cases 2–3 (see Fig. 8) and homogeneous ignition in Cases 4–6 (see Fig. 9) at pressures up to 6 bar. Moreover, as reflected by the locations of  $x_{ig}$  (defined as the far-upstream axial locations where OH attained 5% of its peak value in the channel) in Fig. 9 and Table 3, the catalytic reaction mechanism developed herein improved noticeably the predictions of homogeneous ignition by 2.1–5.2%, compared to the one-step catalytic chemistry in [23], because chemical coupling between the catalytic/gaseous reaction pathways via intermediate species (primarily  $CO$ ) was accounted for when the detailed surface chemistry was used. The minimal effects of radical exchange between the catalytic and gaseous reaction pathways were further investigated by augmenting the mechanism of Table 1 with 6 adsorp-

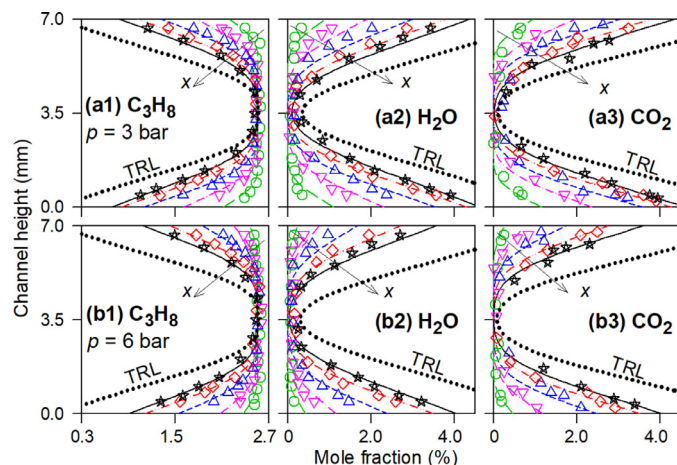


**Fig. 8.** Raman measured (symbols) and simulated (lines) transverse profiles of  $C_3H_8$ ,  $H_2O$  and  $CO_2$  for Cases 2 (a1–a3) and 3 (b1–b3) at pressures of 3 and 6 bar, respectively. Notations as in Fig. 7.

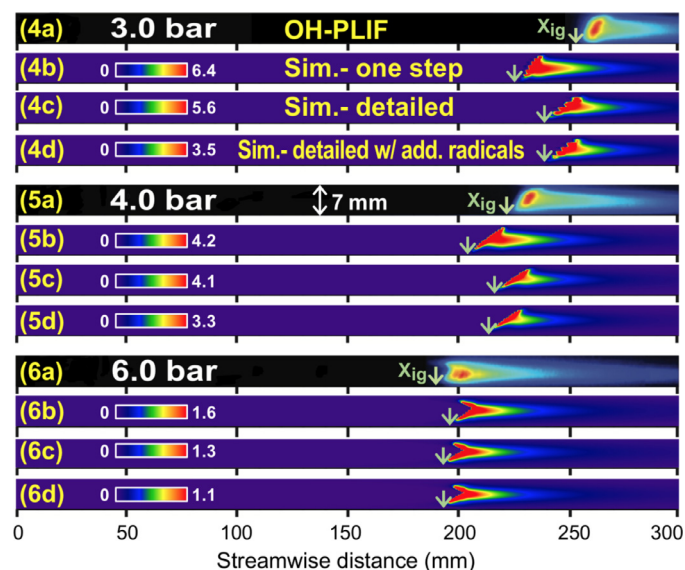


**Fig. 9.** 2D OH distributions for Cases 4–6: (a) OH-PLIF measurements [23], (b) simulations using a one-step catalytic chemistry [23], (c) simulations using the detailed catalytic reaction mechanism of Table 1, and (d) simulations using the detailed catalytic reaction mechanism of Table 1 and additional reactions of O/H/OH adsorption/desorption from [45]. The color bars provide the predicted OH levels ( $10^3$  ppmv).  $x_{ig}$  denotes locations of homogeneous ignition.

tion/desorption steps of O, H, and OH on Rh from [45] (these radical reactions were not part of the original mechanism in [30]). As shown with the locations of  $x_{ig}$  in Figs. 9(4d–6d) and the percentage differences of  $x_{ig}$  in Table 3, with the additional radical steps the homogeneous ignition was practically unaffected in Cases 4 and 6 and slightly overestimated (by  $\sim 0.9\%$ ) in Case 5.

## 5. Further discussion: catalytic ignition and homogeneous ignition during hetero-/homogeneous combustion

Hetero-/homogeneous (i.e. coupled catalytic/gaseous) combustion is of interest in many industrial applications [46]. A major issue of importance during such processes is the ignition of homogeneous combustion. Hence, with the catalytic reaction mechanism developed herein for the total oxidation of  $C_3H_8$  on Rh, homogeneous ignition during hetero-/homogeneous combustion and the controlling surface and gas-phase reactions are numerically investigated. Moreover, it has been shown that under certain conditions



**Table 2**  
Experimental and simulation conditions\*.

Case	$p$	$\varphi$	$U_{IN}$	$T_{IN}$	$C_3H_8$	$O_2$	$N_2$	$T_w$
1	1	0.248	3.94	369	2.56	52.40	45.04	800–1021
2	3	0.248	1.24	347	2.56	52.40	45.04	767–990
3	6	0.248	0.60	335	2.56	52.40	45.04	688–932
4	3	0.524	0.49	390	2.97	27.92	69.11	809–1119
5	4	0.500	0.35	374	2.75	27.98	69.27	763–1107
6	6	0.375	0.23	365	2.07	28.34	69.59	777–1131

\* Pressure (bar), equivalence ratio, inlet velocity (m/s), inlet temperature (K), inlet volumetric compositions (%), and measured wall temperatures (K).

**Table 3**  
Homogeneous ignition distances\*.

Case	$x_{ig,exp}$	GS		DM		DM-aug.	
		$x_{ig,sim}$	$\Delta x_{ig}$	$x_{ig,sim}$	$\Delta x_{ig}$	$x_{ig,sim}$	$\Delta x_{ig}$
4	253	226	+10.7	239	+5.5	239	+5.5
5	222	205	+7.7	216	+2.7	214	+3.6
6	190	197	-3.7	193	-1.6	193	-1.6

\* Measured and simulated ("GS" with the global step of [23], "DM" with the detailed reaction mechanism of Table 1, and "DM-aug." with the detailed reaction mechanism of Table 1 augmented by adsorption/desorption steps of O, H, and OH on Rh from [45]) homogeneous ignition distances (mm) for Cases 4–6. Percentage difference  $\Delta x_{ig} = 100 \times (x_{ig,exp} - x_{ig,sim})/x_{ig,exp}$ .

species exchange between the gaseous and catalytic pathways (via adsorption/desorption reactions) can play a crucial role in the onset of homogeneous ignition [47], which cannot be accounted for when a global catalytic step instead of a detailed surface reaction mechanism is used in the simulations.

To decouple chemical from transport effects, the heterogeneous/homogeneous combustion was investigated using a surface perfectly stirred reactor (SPSR [48], ANSYS Chemkin 2021 R1). Both detailed catalytic (Table 1, together with the global pressure dependence  $p^{-0.86}$  of Eq. (7) [23], which was multiplied for all surface reaction rates in the simulations) and gas-phase [31] reaction mechanisms were used. Inlet gas fractions were taken from Case 6 in Table 2. The surface-to-volume ratio was set as unity and the reactor temperature was kept constant at 1000 K. Two pressures 1 bar and 6 bar were simulated, pertaining to catalytic microre-

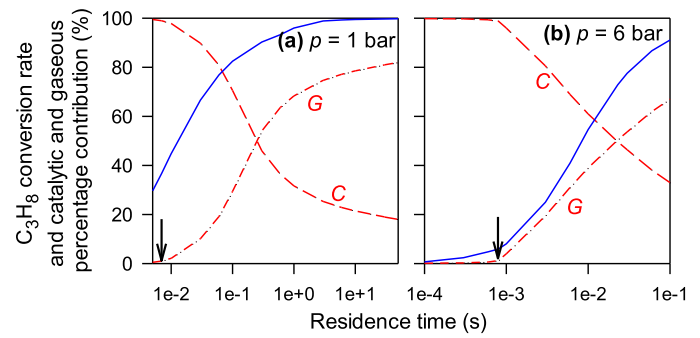


**Fig. 10.** Computed  $C_3H_8$  conversion rates (solid lines) and percentage contribution of catalytic (C, dashed lines) and gaseous (G, dotted-dashed lines) pathways in the  $C_3H_8$  conversion in an SPSR as a function of residence time at two pressures (a) 1 and (b) 6 bar, respectively. The vertical arrows denote when G contributes to 1% of the combined C + G  $C_3H_8$  conversion.

actor and small-scale turbine applications, respectively. As shown with the gaseous (G) contribution of  $C_3H_8$  conversion in Fig. 10, homogeneous ignition was facilitated at higher pressures, despite the fact that the catalytic reactivity was also promoted with rising pressure. At 1 bar, with a residence time of 7 ms (see the vertical arrow in Fig. 10(a)) the gaseous pathway contributed to 1% of the combined C + G ( $C$ : catalytic,  $G$ : gaseous)  $C_3H_8$  conversion and this was considered as the homogeneous ignition point. The gaseous pathway became equally strong as the catalytic pathway when the residence time was increased to 0.24 s (see the crossover of C and G curves). In contrast, at 6 bar, the gaseous pathway contributed to 1% of the C + G  $C_3H_8$  conversion at a much lower residence time 0.8 ms (when the total  $C_3H_8$  conversion was only 5.9% due to such low residence time), and reached 50% with a residence time of 23 ms.

The controlling surface and gaseous reactions were subsequently identified via sensitivity analysis on the  $C_3H_8$  conversion; the 12 most significant reactions of each reaction pathway are shown in Fig. 11 for the 6 bar case of Fig. 10(b). Two residence times were selected, corresponding to when homogeneous combustion was just ignited (0.8 ms) and when it became as vigorous as the catalytic combustion (23 ms). As shown in Fig. 11(a), when

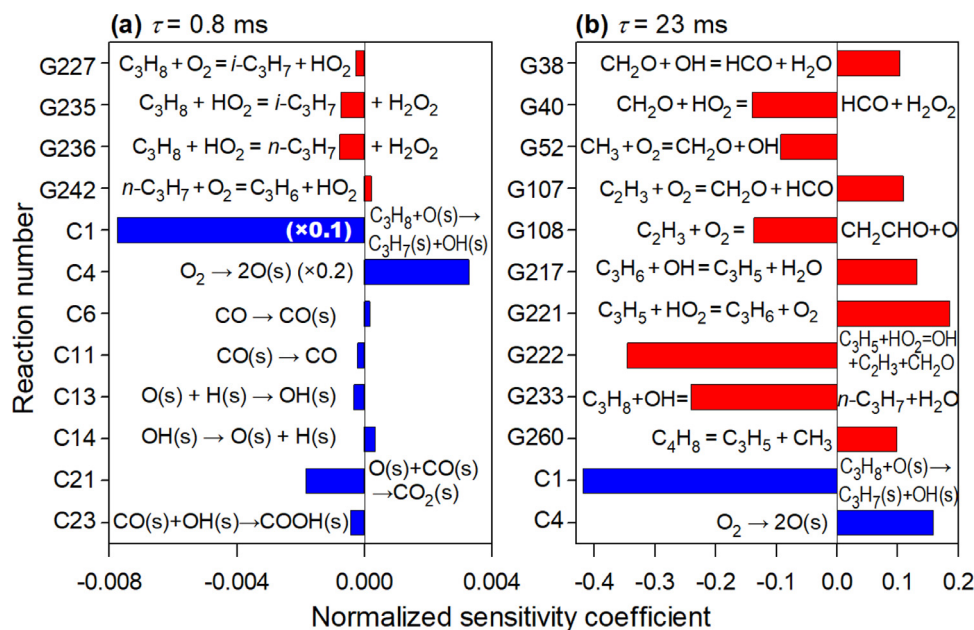


**Fig. 11.** Normalized sensitivity coefficients of  $C_3H_8$  conversion for the 6 bar case in Fig. 10(b) with two residence times (a) 0.8 ms and (b) 23 ms.



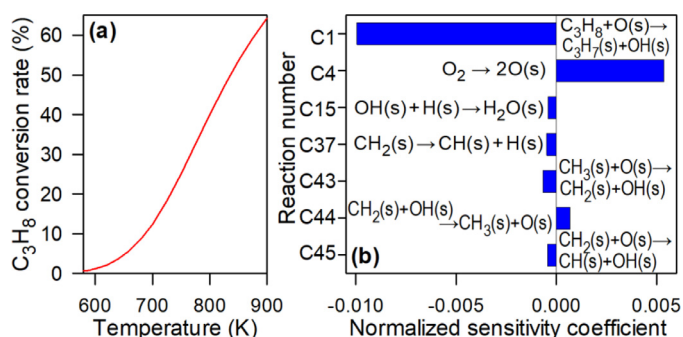


**Fig. 12.** (a) Conversion rate of 1% vol. C<sub>3</sub>H<sub>8</sub> in air in an atmospheric SPSR over the temperature range 580–900 K. (b) Controlling reactions during catalytic ignition at 580 K.

homogeneous combustion was just ignited, the dehydrogenation steps of C<sub>3</sub>H<sub>8</sub> via HO<sub>2</sub> (G235 and G236) and O<sub>2</sub> (G227) were the most important gas-phase reactions facilitating C<sub>3</sub>H<sub>8</sub> consumption. At this point, the C<sub>3</sub>H<sub>8</sub> conversion was overwhelmingly controlled by catalytic reactions, with C1 (dissociative adsorption of C<sub>3</sub>H<sub>8</sub>) and C4 (adsorption of O<sub>2</sub>) being the dominating ones. C4 has a positive sensitive coefficient and hence a hindering role on C<sub>3</sub>H<sub>8</sub> conversion, reflecting the competition between the two reactants for surface adsorption. When the residence time was increased to 23 ms in Fig. 11(b), the gaseous pathway caught up with the catalytic pathway in C<sub>3</sub>H<sub>8</sub> conversion. All the gaseous and catalytic reactions in Fig. 11(a), except C1 and C4, became insignificant. C1 was still the most important in consuming C<sub>3</sub>H<sub>8</sub>, closely followed by gaseous reactions G222 and G233. On the other hand, G221 exceeded C4 as the most inhibiting reaction for C<sub>3</sub>H<sub>8</sub> conversion. The augmented adsorption/desorption steps for the O, H, and OH radicals (see Section 4) were not important in both cases when they were included in the SPSR simulations, and hence would not show in Fig. 11.

Finally, the reactions controlling catalytic ignition were also identified using an SPSR, with only catalytic chemistry and without gas-phase chemistry. The inlet mixture was 1% vol. C<sub>3</sub>H<sub>8</sub> doped in air and at 1 bar, mimicking the wire microcalorimetry experiments. The residence time was fixed at 0.1 s, while the reactor temperature was altered from 580 to 900 K. As shown in the plot of fuel conversion as a function of temperature in Fig. 12(a), nearly 1% of the C<sub>3</sub>H<sub>8</sub> was converted at 580 K, which was considered as the catalytic ignition temperature. This result was close to the measured ignition temperature 585 K in the wire microcalorimetry experiments, when minimal detectable heat release was recorded. The controlling reactions at 580 K in the SPSR are given in Fig. 12(b). C1 and C4 were again the most significant reactions, competing for surface adsorption. Other important promoting reactions included the generation of H<sub>2</sub>O(s) (C15), and dehydrogenation of CH<sub>3</sub> to CH<sub>2</sub> (C44) and CH<sub>2</sub> to CH (C37 and C45), while the second strongest inhibiting reaction was C44 (CH<sub>2</sub>(s) + OH(s) → CH<sub>3</sub>(s) + O(s)).

## 6. Conclusions

The total oxidation of C<sub>3</sub>H<sub>8</sub> over Rh was experimentally and numerically investigated using wire microcalorimetry experiments, surface characterization, CFD and SPSR simulations with detailed catalytic and gaseous reaction mechanisms. The global catalytic reaction parameters were first extracted from heat release measurements in an atmospheric wire microcalorimeter within the kinetic-controlled regime, based on which two lumped reactions of C<sub>3</sub>H<sub>8</sub> dissociative adsorption and its subsequent surface decomposition were fitted. By further incorporating these two steps into a CH<sub>4</sub>-Rh model, a detailed and thermodynamically-consistent catalytic reac-

tion mechanism for the total oxidation of C<sub>3</sub>H<sub>8</sub> over Rh was constructed. The developed reaction mechanism not only reproduced the heat release rates in the wire microcalorimetry experiments, but was also validated against 2D Raman measurements of major gas-phase species concentrations in an Rh-coated planar channel-flow reactor.

When considering a recently reported pressure dependence of the reaction pre-exponentials, the catalytic reaction mechanism developed excellently captured catalytic reactivity and homogeneous ignition during coupled hetero-/homogeneous combustion at pressures up to 6 bar. It was found that the exchange of reaction intermediates (primarily CO) between the catalytic and gaseous reaction pathways played an appreciable role in the ignition of homogeneous combustion. On the other hand, the addition of radical (O, H and OH) adsorption/desorption reactions had a minimal impact on homogeneous ignition. Finally, key reactions controlling catalytic ignition and homogeneous ignition during hetero-/homogeneous combustion were identified using SPSR simulations. In all cases, the most important catalytic reactions were the adsorption steps of C<sub>3</sub>H<sub>8</sub> and O<sub>2</sub>, which competed for surface free sites. For catalytic ignition, CH<sub>3</sub>(s) to CH<sub>2</sub>(s) and CH<sub>2</sub>(s) to CH(s) were also important, while the homogeneous ignition during hetero-/homogeneous combustion was controlled by the dehydrogenation steps of C<sub>3</sub>H<sub>8</sub> via HO<sub>2</sub> and O<sub>2</sub>.

## Declaration of Competing Interest

The authors declare that they have no known competing financial interests or personal relationships that could have appeared to influence the work reported in this paper.

## Acknowledgments

The wire microcalorimetry experiments were performed at Princeton University, supported by the US Army Research Office (Grant #W911NF1910038). RS acknowledges a faculty startup fund from Missouri University of Science and Technology. JM acknowledges support from the EU Horizon-2020 project NextMGT. The plate reactor tests were supported by the Swiss Federal Office of Energy (BFE) under project SI/501976-01.

## References

- [1] A. Gerini, G. Monnier, R. Bonetto, Ultra low emissions vehicle using LPG engine fuel, SAE Technical Paper, (1996) No. 961079.
- [2] T.Y. Kim, C. Park, S. Oh, G. Cho, The effects of stratified lean combustion and exhaust gas recirculation on combustion and emission characteristics of an LPG direct injection engine, *Energy* 115 (2016) 386–396.
- [3] J. Wan, A. Fan, Recent progress in flame stabilization technologies for combustion-based micro energy and power systems, *Fuel* 286 (2021) 119391.
- [4] S. Karagiannidis, J. Mantzaras, K. Boulouchos, Stability of hetero-/homogeneous combustion in propane and methane fueled catalytic microreactors: channel confinement and molecular transport effects, *Proc. Combust. Inst.* 33 (2011) 3241–3249.
- [5] S. Karagiannidis, K. Marketos, J. Mantzaras, R. Schaeren, K. Boulouchos, Experimental and numerical investigation of a propane-fueled, catalytic mesoscale combustor, *Catal. Today* 155 (2010) 108–115.
- [6] T.A. Wierzbicki, I.C. Lee, A.K. Gupta, Combustion of propane with Pt and Rh catalysts in a meso-scale heat recirculating combustor, *Appl. Energy* 130 (2014) 350–356.
- [7] Technical Overview of Volatile Organic Compounds, US Environmental Protection Agency, accessed in August 2021 <https://www.epa.gov/indoor-air-quality-iaq/technical-overview-volatile-organic-compounds#8> accessed in.
- [8] Z.Y. Tian, P.H.T. Ngamou, V. Vannier, K. Kohse-Höinghaus, N. Bahlawane, Catalytic oxidation of VOCs over mixed Co–Mn oxides, *Appl. Catal. B-Environ.* 117 (2012) 125–134.
- [9] J.J. Harrison, P.F. Bernath, Infrared absorption cross sections for propane (C<sub>3</sub>H<sub>8</sub>) in the 3 μm region, *J. Quant. Spectrosc. Radiat. Transf.* 111 (2010) 1282–1288.
- [10] D. Helmig, S. Rossabi, J. Hueber, P. Tans, S.A. Montzka, K. Masarie, K. Thoning, C. Plass-Duelmer, A. Claude, L.J. Carpenter, A.C. Lewis, Reversal of global atmospheric ethane and propane trends largely due to US oil and natural gas production, *Nat. Geosci.* 9 (2016) 490–495.

- [11] H. Xu, N. Yan, Z. Qu, W. Liu, J. Mei, W. Huang, S. Zhao, Gaseous heterogeneous catalytic reactions over Mn-based oxides for environmental applications: a critical review, *Environ. Sci. Technol.* 51 (2017) 8879–8892.
- [12] K. Kohse-Höinghaus, Combustion in the future: the importance of chemistry, *Proc. Combust. Inst.* 38 (2021) 1–56.
- [13] C.P. O'Brien, G.R. Jenness, H. Dong, D.G. Vlachos, I.C. Lee, Deactivation of Pt/Al<sub>2</sub>O<sub>3</sub> during propane oxidation at low temperatures: kinetic regimes and platinum oxide formation, *J. Catal.* 337 (2016) 122–132.
- [14] T.F. Garetto, E. Rincón, C.R. Apesteguía, Deep oxidation of propane on Pt-supported catalysts: drastic turnover rate enhancement using zeolite supports, *Appl. Catal. B-Environ.* 48 (2004) 167–174.
- [15] M. Bhagiyalakshmi, R. Anuradha, S.D. Park, T.S. Park, W.S. Cha, H.T. Jang, Effect of bimetallic Pt-Rh and trimetallic Pt-Pd-Rh catalysts for low temperature catalytic combustion of methane, *Bull. Korean Chem. Soc.* 31 (2010) 120–124.
- [16] X. Dong, K. Tsuneyama, T. Hibino, Ultra-low loading Pt-Rh/Sn<sub>0.9</sub>In<sub>0.1</sub>P<sub>2</sub>O<sub>7</sub> three-way catalyst for propane + NO + O<sub>2</sub> reaction, *Appl. Catal. B-Environ.* 106 (2011) 503–509.
- [17] A. Maione, F. Andre, P. Ruiz, The effect of Rh addition on Pd/ $\gamma$ -Al<sub>2</sub>O<sub>3</sub> catalysts deposited on FeCrAlloy fibers for total combustion of methane, *Appl. Catal. A-Gen.* 333 (2007) 1–10.
- [18] M.S.L. Aparicio, M.A. Ocsachoque, E. Rodríguez-Castellón, D. Gazzoli, M.L. Casella, I.D. Lick, Promoting effect of rhodium on Co/ZnAl<sub>2</sub>O<sub>4</sub> catalysts for the catalytic combustion of hydrocarbons, *Catal. Today* 372 (2021) 2–10.
- [19] R. Sui, J. Mantzaras, R. Bombach, A comparative experimental and numerical investigation of the heterogeneous and homogeneous combustion characteristics of fuel-rich methane mixtures over rhodium and platinum, *Proc. Combust. Inst.* 36 (2017) 4313–4320.
- [20] D. Livio, A. Donazzi, A. Beretta, G. Groppi, P. Forzatti, Experimental and modeling analysis of the thermal behavior of an autothermal C<sub>3</sub>H<sub>8</sub> catalytic partial oxidation reformer, *Ind. Eng. Chem. Res.* 51 (2012) 7573–7583.
- [21] C. Karakaya, H. Karadeniz, L. Maier, O. Deutschmann, Surface reaction kinetics of the oxidation and reforming of propane over Rh/Al<sub>2</sub>O<sub>3</sub> catalysts, *ChemCatChem* 9 (2017) 685–695.
- [22] D. Pagani, D. Livio, A. Donazzi, A. Beretta, G. Groppi, M. Maestri, E. Tronconi, A kinetic analysis of the partial oxidation of C<sub>3</sub>H<sub>8</sub> over a 2% Rh/Al<sub>2</sub>O<sub>3</sub> catalyst in annular microreactor, *Catal. Today* 197 (2012) 265–280.
- [23] J. Mantzaras, R. Sui, C.K. Law, R. Bombach, Heterogeneous and homogeneous combustion of fuel-lean C<sub>3</sub>H<sub>8</sub>/O<sub>2</sub>/N<sub>2</sub> mixtures over rhodium at pressures up to 6 bar, *Proc. Combust. Inst.* 38 (2021) 6473–6482.
- [24] R. Sui, W. Liang, L. Zhang, J. Mantzaras, C.K. Law, Kinetic interactions between H<sub>2</sub> and CO in catalytic oxidation over PdO, *Combust. Flame* 211 (2020) 270–280.
- [25] T.C. Zhang, D.L. Zhu, N. Yao, F. Qi, C.K. Law, A wire microcalorimetric study of catalytic ignition of methane-air mixtures over palladium oxide, *Proc. Combust. Inst.* 33 (2011) 1819–1825.
- [26] Y.X. Xin, S. Lieb, H. Wang, C.K. Law, Kinetics of catalytic oxidation of methane over palladium oxide by wire microcalorimetry, *J. Phys. Chem. C* 117 (2013) 19499–19507.
- [27] J.W. Arblaster, Selected electrical resistivity values for the platinum group of metals Part II: rhodium and iridium, *Johnson Matthey Technol. Rev.* 60 (2016) 4–11.
- [28] Y.X. Xin, H. Wang, C.K. Law, Kinetics of catalytic oxidation of methane, ethane and propane over palladium oxide, *Combust. Flame* 161 (2014) 1048–1054.
- [29] T.C. Zhang, Y.X. Xin, Z.Y. Ren, F. Qi, C.K. Law, Catalytic oxidation of methane over PdO in wire microcalorimetry, *Combust. Flame* 160 (2013) 149–154.
- [30] C. Karakaya, L. Maier, O. Deutschmann, Surface reaction kinetics of the oxidation and reforming of CH<sub>4</sub> over Rh/Al<sub>2</sub>O<sub>3</sub> catalysts, *Int. J. Chem. Kinet.* 48 (2016) 144–160.
- [31] UC San Diego chemical reaction mechanism (version 2016-12-14). <https://web.eng.ucsd.edu/mae/groups/combustion/mechanism.html>, accessed in August 2021.
- [32] M. Reinke, J. Mantzaras, R. Schaeren, R. Bombach, A. Inauen, S. Schenker, High-pressure catalytic combustion of methane over platinum: in situ experiments and detailed numerical predictions, *Combust. Flame* 136 (2004) 217–240.
- [33] Y. Abe, K. Kato, M. Kawamura, K. Sasaki, Rhodium and rhodium oxide thin films characterized by XPS, *Surf. Sci. Spectra* 8 (2001) 117–125.
- [34] D. Ciuparu, M.R. Lyubovskiy, E. Altman, L.D. Pfefferle, A. Datye, Catalytic combustion of methane over palladium-based catalysts, *Catal. Rev.* 44 (2002) 593–649.
- [35] M. Hartmann, L. Maier, H.D. Minh, O. Deutschmann, Catalytic partial oxidation of iso-octane over rhodium catalysts: an experimental, modeling, and simulation study, *Combust. Flame* 157 (2010) 1771–1782.
- [36] Y.X. Xin, B. Yang, H. Wang, S.L. Anderson, C.K. Law, Kinetics of catalytic oxidation of ethylene over palladium oxide, *Proc. Combust. Inst.* 35 (2015) 2233–2240.
- [37] J. Mantzaras, Catalytic combustion of syngas, *Combust. Sci. Technol.* 180 (2008) 1137–1168.
- [38] J. Mantzaras, Transient modeling in heterogeneous combustion, in: G.I. Stoev (Ed.), *Heterogeneous Combustion*, Nova Science Publ., New York (2011), pp. 1–75.
- [39] T. Shimizu, A.D. Abid, G. Poskrebyshv, H. Wang, J. Nabity, J. Engel, J. Yu, D. Wickham, B. Van Devener, S.L. Anderson, S. Williams, Methane ignition catalyzed by in situ generated palladium nanoparticles, *Combust. Flame* 157 (2010) 421–435.
- [40] R. Sui, J. Mantzaras, R. Bombach, H<sub>2</sub> and CO heterogeneous kinetic coupling during combustion of H<sub>2</sub>/CO/O<sub>2</sub>/N<sub>2</sub> mixtures over rhodium, *Combust. Flame* 202 (2019) 292–302.
- [41] R. Sui, E. Es-sebbar, J. Mantzaras, R. Bombach, Homogeneous ignition during fuel-rich H<sub>2</sub>/O<sub>2</sub>/N<sub>2</sub> combustion in platinum-coated channels at elevated pressures, *Combust. Flame* 180 (2017) 184–195.
- [42] M.E. Coltrin, R.J. Kee, F.M. Rupley, Surface Chemkin: A Fortran Package for Analyzing Heterogeneous Chemical Kinetics at the Solid Surface-Gas Phase Interface, Report No. SAND90-8003C, Sandia National Laboratories, USA, 1996 Report No. SAND90-8003C.
- [43] R.J. Kee, F.M. Rupley, J.A. Miller, Chemkin II: A Fortran chemical kinetics package for the analysis of gas-phase chemical kinetics, Report No. SAND89-8009B, Sandia National Laboratories, USA, 1996.
- [44] R.J. Kee, G. Dixon-Lewis, J. Warnatz, M.E. Coltrin, J.A. Miller, A Fortran computer code package for the evaluation of gas-phase multicomponent transport properties, Report No. SAND86-8246, Sandia National Laboratories, USA, 1996.
- [45] M. Maestri, D.G. Vlachos, A. Beretta, G. Groppi, E. Tronconi, A C<sub>1</sub> microkinetic model for methane conversion to syngas on Rh/Al<sub>2</sub>O<sub>3</sub>, *AIChE J.* 55 (2009) 993–1008.
- [46] J. Mantzaras, Progress in non-intrusive laser-based measurements of gas-phase thermoscalars and supporting modeling near catalytic interfaces, *Prog. Energy Combust. Sci.* 70 (2019) 169–211.
- [47] R. Sui, W. Liang, J. Mantzaras, C.K. Law, Coupled reaction mechanism reduction for the hetero-/homogeneous combustion of syngas over platinum, *Combust. Flame* 214 (2020) 37–46.
- [48] H.K. Moffat, R.J. Kee, J.F. Grcar, J.A. Miller, Surface PSR: a Fortran program for modeling well-stirred reactors with gas and surface reactions, Report No. SAND91-8001, Sandia National Laboratories, USA, 1993.